Oxidation behavior of chromium-rich Fe-based alloys containing HfC carbides at 1100 °C

Elodie Conrath, Patrice Berthod

Oxidation behavior of chromium-rich Fe-based alloys containing HfC carbides at 1100 °C

Elodie Conrath and Patrice Berthod

Institut Jean Lamour (UMR CNRS 7198), department Chemistry and Physic of Solids and Surfaces
Faculty of Science and Technologies, B.P. 70239, 54506 Vandoeuvre-lès-Nancy, France

E-mail: pberthodcentralelille1987@orange.fr

Tel. (+33) 3 72 74 27 29

Post-print version of the article: **Materials and Corrosion (2015) 66, No.10, pp.1101–1110.**
DOI: 10.1002/maco.201407916

Summary:
Three HfC-containing iron-based alloys were successfully elaborated by foundry. The alloys, all containing 27wt.%Cr, 0.25 or 0.50wt.%C and 4 to 6wt.%Hf, are composed of a dendritic matrix and of HfC carbides of two types: pre-eutectic blocky carbides and interdendritic script-like HfC carbides. These alloys were subjected to thermogravimetry tests in air at 1100°C for 46 hours. The presence of hafnium led to oxidation kinetics globally parabolic and low mass gain rates, by comparison with similar Hf-free ternary alloys. The scales formed all over the samples' surfaces were never composed exclusively of chromia. Iron oxides or (iron, chromium) oxides were also present. Some particles of hafnium oxides were noticed in the subsurface and in the external scales. These particles obviously pegged the external oxide scale on the alloy surface. The long exposure at this high temperature did not significantly modify the characteristics of the bulk HfC carbides. For the alloys in which they were present in the as-cast state, the eutectic chromium carbides played an important role. They dissolved and helped to supply chromium by enriching the interdendritic spaces which act as fast diffusion paths. In the alloy containing 0.50 wt.%Cr and 4 wt.%Hf, a parabolic constant of only 2.5×10^{-10} $g^2 \times cm^{-4} \times s^{-1}$ was thus obtained, which is a very low value for 1100°C.

Keywords:
Iron alloys; Hafnium carbides; High temperature Oxidation; Thermogravimetry tests; Post-mortem characterization

1 Introduction

Many applications need materials able to long lasting uses at high temperature under mechanical stresses in presence of either oxidant gases or aggressive liquids (e.g. molten salts). Ductility high enough and good impact toughness may be obtained when metallic alloys are selected. The complex geometry of many of the hot pieces used at elevated temperatures leads to prefer casting as elaboration route for these alloys. Additionally this technique allows obtaining coarse-grained microstructures which are favorable to high strength at high temperature [1]. A good resistance against high temperature oxidation may be achieved by addition of aluminum, chromium or silicon to the alloys [2]. Chromium is often considered, not necessarily as the best element for oxidation resistance, but as being a good compromise for the resistance against both oxidation by gases and corrosion by molten substances [3]. On the other hand, inversely, the high temperature alloys which are rich in chromium must be rather poor in aluminum to avoid metallurgical instabilities at high temperature. Consequently they cannot be strengthened by gamma prime precipitates as the γ/γ' − single crystal nickel−based superalloys which are often considered as the best existing superalloys [4].

Alloys used as complex−shaped pieces for high temperature service under mechanical stresses and in corrosive environments (gaseous and liquid) must be reinforced by solid solution strengthening and/or by precipitation of hard particles. Among the latter ones there are carbides. Unfortunately these ones are not all stable enough at high temperature to allow providing the alloys an efficient strengthening on long times at temperatures significantly higher than 1000°C. Indeed, at high temperature the chromium carbides, which are frequently used to strengthen superalloys, tend to coalesce, to become rarer and even to disappear. The tantalum carbides are also commonly used for the reinforcement of superalloys. For that, the script−like shape of these TaC carbides, as well as the mix between the eutectic TaC and the matrix in the interdendritic spaces, allow them bringing high creep−resistance.

But, at very high temperature, the TaC carbides are affected by morphologic evolutions and by the decrease of their volume fraction. Among the other MC carbides, there are also hafnium carbides. As verified in a previous work [5] for a chromium−rich cobalt−based alloy, these HfC carbides may precipitate during solidification with the same script−like shape as the TaC carbides. Furthermore they form also a eutectic compound with the matrix. Additionally, the HfC carbides seemed to be significantly more resistant against morphologic evolution during long stages at high temperature. This allows their strengthening potential being maintained at a high level on long times.

Using HfC carbides for the mechanical reinforcement of alloys at high temperature was obviously chosen in some rare cases. Indeed, there are only few published works which deal with the strengthening of alloys with HfC: some of them concern Ni−based [6] and Co−based [7] metallic materials (hard metals or superalloys), other ones molybdenum−based [8] or tungsten−based [9] alloys. The improvement of the tensile properties [10] or of the creep resistance [11] by hafnium carbides was applied for (molybdenum, tungsten) −based alloys or (tungsten, rhenium)-based alloys [12-14].

Iron, with its particularly high melting point (1535°C) [15] and its low cost, may be considered as an interesting base element for refractory alloys. Its poor mechanical resistance at high temperature may be possibly greatly improved by an efficient strengthening by hafnium carbides.

Such association of a very refractory chromium−rich iron base with a reinforcing network of hafnium carbides (which needs several weight percent of hafnium) is rather original. Indeed hafnium is generally only added with the typical amount of 1wt.%Hf or less, exclusively for improving the high temperature oxidation behavior of the alloys. With the contents used in the alloys considered in this work (4 wt.% and more) one may wonder whether the presence of hafnium will be still beneficial for the high temperature oxidation behavior of the alloys. Furthermore one may fear that so high contents in this very oxidable element possibly lead to a detrimental effect, on the contrary. The purpose of this work is precisely to characterize this behavior at 1100°C, typical temperature of use to which such alloys are destined.

2 Experimental details

2.1 Synthesis of the alloys

Three Hf-containing iron−based alloys were synthesized by foundry. The following compositions were targeted: 27 wt.%Cr, 0.25 or 0.50 wt.%C, and 4 or 6 wt.%Hf. In parallel, for evidencing the influence of these high Hf contents on the high temperature oxidation behavior, two Hf-free ternary alloys containing the same chromium and carbon quantities were also elaborated and tested. For each alloy pure elements (Alfa Aesar, purity > 99.9wt.%) were melted together in a High Frequency induction furnace (CELES). Heating, melting, solidification and solid state cooling took place in a closed silica tube containing an inert atmosphere of pure argon (300mbars). Five compact 40g-weighing ingots were obtained. After return to ambient temperature, the ingots were cut in order to obtain two types of sample: metallographic samples devoted to the examination of the as-cast microstructures, and parallelepiped samples for the thermogravimetry tests (dimensions: about 10 × 10 × 3 mm^3). The samples for metallography were embedded in a cold resin mixture (resin CY230 + hardener

HY956, ESCIL). They were ground by using SiC−enriched papers with grade varying from 120 to 1200. Using ultrasonic vibrations in water, the metallographic samples were cleaned to allow further polishing without pollution by hard particles. Finishing was done by using textile containing 1µm−alumina particles. A mirror−like state was thus achieved for all the metallographic samples to allow their examination using optical and electron microscopes.

2.2 The 1100°C−oxidation runs

The parallelepiped samples destined to the oxidation tests in thermo−balance were ground with SiC−papers (120 to 1200−grit). Their edges and corners were smoothed using 1200−grit paper. They were oxidized in a SETARAM TGA92 thermo−balance which allows recording the mass variation versus time. The thermal cycle was applied in dry synthetic air (80%N_2 – 20%O_2). It was composed of a heating at +20°C/min, an isothermal stage of 46 hours at 1100°C and a cooling rate at -5°C/min. The mass gain files were plotted versus time to see whether the kinetic was parabolic or not. The mass gain per surface unit area (noted m) was thereafter plotted versus the square root of time to determine the parabolic constant Kp according to the classical method. When chromia is the major oxide to develop, a so high temperature as 1100°C may induce the volatilization of this oxide by favoring its new oxidation into the new CrO_3 oxide which is gaseous at this temperature. This must be taken into account in order to avoid minimizing the oxidation rate when this one is assessed by mass gain recording. The curves which display an almost parabolic shape and which are regular enough were exploited again by applying a second method. They were analyzed according to the $\{m \times dm/dt = Kp - Kv \times m\}$ method [16] in order to simultaneously specify the parabolic constant Kp without any underestimation, and the chromia volatilization constant Kv. The curve obtained by plotting the $m \times dm/dt$ quantity versus -m (where m is the mass gain per surface unit area) appears linear for values of time high enough (i.e. after the end of the transient oxidation). The two kinetic constants can be then red in the equation of this straight line: the chromia volatilization constant Kv is simply the slope, and the parabolic constant Kp is its ordinate at the origin. This method is applicable even if iron is present with chromium in the external M_2O_3 (M=Cr and/or Fe) scale but only if this scale is continuous all around the sample.

2.3 Post-mortem characterization

After the oxidation runs, the oxidized samples were characterized by metallography observations and analyses. The oxidized surfaces were first scanned using a simple office scanner, to value the oxide spallation occurred during cooling. Second, X-Ray diffraction runs were performed on the oxidized surfaces by using a Philips X'Pert Pro diffractometer, to identify the natures of the external oxides formed on the surfaces of the samples.

Thereafter a thin gold layer was deposited all around the oxidized samples by cathodic evaporation. A thick electrolytic layer of nickel was then deposited to prevent any loss of the external oxide during cutting. After that, the coated oxidized samples were cut in two parts, embedded in a cold resin mixture, ground and polished until obtaining a mirror−like surface. The cross−sections were examined by using a Scanning Electron Microscope (SEM) JEOL JSM-6010LA in the Back Scattered Electrons (BSE) mode. Local analyses using the Energy Dispersion Spectrometry (EDS) apparatus equipping the SEM were performed in the oxide scales to specify the different types of oxides and to measure the chemical compositions in the alloy very close to the oxide / alloy interface. Additionally, EDS profiles were performed using the same apparatus to characterize the possible chromium or hafnium depletion zones in the sub-surface.

3 Results

3.1 Chemical compositions and microstructures of the obtained alloys

After their elaboration the ingots were cut to obtain parts which allow characterizing the alloys in their as−cast state. During the SEM/BSE observations at the ×1000 magnification of the mounted and polished samples, EDS measurements were performed on the whole areas for knowing the real chemical compositions. By looking at the results given in Table 1 one can see that all the alloys have seemingly the same chromium content. This one is in all cases of about 27 wt.%, close to the targeted value. Concerning the hafnium contents two levels were obtained: 4 and 6 wt.%.

The microstructures of the Hf−containing alloys in their as−cast state are illustrated by the SEM/BSE micrographs presented in Figure 1. The matrix of each alloy is composed of a solid solution of iron-chromium, the morphology of which is dendritic. In the interdendritic spaces the matrix is mixed with eutectic HfC carbides. These ones appear as white particles when observed with the SEM in BSE mode. Other HfC carbides can be also observed: they are cubic or polygonal white particles, which are neither present homogenously in the microstructure, nor systematically present in the interdendritic spaces (in contrast with the eutectic HfC). They seem having crystallized at the early beginning of solidification when the temperature was still very high, together with dendrites. The hafnium carbides of this second type will be thereafter called "pre-eutectic HfC".

The alloy which seems presenting the lowest surface fraction of HfC is logically also one of the two Hf–poorer alloys (Fh50, 4 wt.%Hf). There are also chromium carbides but only in two of the three Hf–containing alloys. No chromium carbides can be seen in the Fh25 alloy because its atomic contents in carbon and in hafnium are similar. Hafnium is a carbide–former element stronger than chromium, and all carbon atoms were involved in the formation of HfC carbides, exclusively. With twice this carbon content for a similar hafnium content the crystallization of chromium carbides besides the HfC ones during solidification was possible for the Fh50 alloy. These chromium carbides are the particles which appear darker than the matrix. With a hafnium content as high as 6 wt.% for the same carbon content as the Fh50 alloy, the chromium carbides are less present in the as-cast FH50 alloy.
To finish with the descriptions of the as–cast microstructures, the two Hf–free alloys, F25 and F50 only contain chromium carbides. These ones are logically more numerous in the second alloy (0.50 wt.% C) than in the first one (0.25 wt.% C).

3.2 Kinetic of oxidation

The obtained mass gain curves are displayed in Figure 2 for the two {0.25 wt.% C} – containing alloys and in Figure 3 for the three {0.50 wt.% C} – containing alloys. After a short rather slow mass gain at the beginning of the isothermal stage, it appears that the oxidation of each of the two Hf-free alloys considerably accelerates. There are notably mass gain jumps which are obviously due to local scale detachments which induced new fast oxidation of the denuded parts of alloy. In contrast, the three Hf–containing alloys oxidize much slower. The mass gain curves of these three alloys are globally parabolic – this indicating that the oxide scale was continuous all around the sample – and their final mass gains after 46 hours are lower than 2 mg × cm^{-2}. The final mass gains for the Fh25 and FH50 alloys are almost the same. One can notice that the oxidation rate of the Fh50 alloy is particularly low.
The five mass gain files were analyzed according to two methods for the determination of the values of the kinetic parabolic constant (Kp) and of the chromia volatilization constant (Kv). Kp was first determined as being the average slope of the straight line obtained by plotting the mass gain versus the square root of time ("classic Kp"). In a second time, the mass loss resulting from the new oxidation of a part of chromia into the volatile CrO_3 new oxide (gaseous at temperature higher than 1000°C) was valued in order to do not risk minimizing the mass gain (and consequently the oxidation rate). For that the mass gain files were plotted as m × dm/dt versus –m (example of the Fh50 alloy given in Figure 4A). When chromia is effectively the main oxide formed, this curve is described by the following equation: m × dm/dt = Kp – Kv × dm. Kp appears as being the ordinate at the origin of the regression straight line and Kv as being its slope (respectively 2.5 × 10^{-12} g^2 × cm^{-4} × s^{-1} and 60 × 10^{-10} g × cm^{-2} × s^{-1} in the presented example: Fh50 alloy). These values must be validated by plotting a mathematical model curve (here by using the Excel software of Microsoft) and by comparing it to the experimental mass gain curve. On the example given in Figure 4B it appears that the model curve ("math Kp & Kv") calculated with the values of the Kp and Kv constants previously determined, perfectly fits the experimental curve ("exp"). It is not the case of the "math Kp classic" model curve plotted with only the Kp value which was classically determined.
The obtained values are listed in Table 2. Even if the shapes of the mass gain curves acquired for the two Hf-free alloys were not parabolic it was decided to get an equivalent value of Kp. The value obtained for the F25 alloy is very high. In the case of the F50 alloy, there was a first short - but globally parabolic - part of the mass gain curve. On this part of the curve a value of Kp (classical method) was obtained. This one is higher than the values of Kp classically determined for the three Hf-free alloys. The same order is observed when the simultaneous determination of both Kp and Kv was done. However the parabolic constants corrected from volatilization of chromia were of the same level for the Hf-free F50 alloy and the Hf-containing Fh25 and FH50 alloys. The Fh50 alloys showed a remarkable oxidation behavior since its Kp value is very low. The value of Kv obtained for this alloy is itself also very low.

3.3 Post-mortem characterization

To help interpret the kinetic results, the oxidized surfaces of the samples were analyzed by X-ray Diffraction before cutting and cross-section preparation. The results are illustrated by the three diffractograms given in Figure 5, Figure 6 and Figure 7. Globally the Hf-free alloys were essentially covered by oxides of both iron and chromium with various ratios between Fe and Cr, but pure chromia is also detected (very small peaks). The scales formed over the Hf–containing alloys are composed of the same oxides of both Fe and Cr (and small quantities of chromia) but one can also notice the presence of hafnium oxide in small quantities. The observations in cross-section (Figure 8) allowed seeing that the scales are much thicker – notably for the F25 alloy – over the Hf–free alloys than over the Hf–containing alloys. But, there were also some locations of fast oxidation for the FH50 alloy (Figure 9). Local EDS measurements were performed in the external oxide, as well as in the internal oxides when present. The identified oxides are pointed out in the micrographs of Figure 8 and

Figure 9. The different oxides, detected by XRD on the oxidized surfaces or specified by EDS on cross-sections, are listed in Table 3.There was a general good agreement but some oxides detected by XRD were not necessarily present on the areas observed with the SEM and analyzed by EDS. Furthermore, in some cases, the XRD diffractograms seemed revealing the presence of the spinel $FeCr_2O_3$ oxide on the oxidized Hf–free alloys and of HfO_2 on the oxidized Hf–containing alloys. However the XRD peaks were rather small and close to the background, and it was not really possible to accurately specify the stoichiometry of the oxides by EDS. Thus one cannot really confirm the presence of the spinel $FeCr_2O_3$ oxide.

As consequences of the continuous scale existing all around the samples and mainly composed of $(Cr,Fe)_2O_3$ is first that the $m \times dm/dt = Kp - Kv \times dm$ method was effectively applicable and second that the obtained values of Kp and Kv are correct.

EDS profiles were additionally performed across the sub-surface affected by oxidation perpendicularly to the oxide/alloy interface (Figure 10). In contrast with what is generally observed for oxidized chromium–rich alloy and observed for the two Hf–free alloys, there are seemingly no chromium–depleted zones in the sub–surfaces of the three Hf–rich alloys. The concentrations profiles are rather horizontal, except when the electron beam reaches a HfC carbide or an internal HfO_2 oxide or nitride.

In the core of the oxidized samples the bulk microstructure has also evolved (Figure 11). For example the chromium carbides have become much rounder in the four alloys in which they were initially present (F25, F50, Fh50 and FH50). In addition, some rare chromium carbides have also precipitated in the Fh25 alloy in which such carbides were not present in the as–cast state. The eutectic HfC carbides have also evolved a little: slight lowering of their apparent surface fraction and slight fragmentation which led to a partial loss of the initial script-like morphology of these carbides.

4 Discussion

The two Hf–free alloys displayed a rather bad behavior in oxidation at 1100°C. They showed first a chromia–forming behavior over the first hours (more precisely a $(Cr,Fe)_2O_3$–forming behavior). But oxidation started to accelerate thereafter. The adherence of the scales on the substrate was not very good for these ternary alloys. This led to local detachments of the scale which exposed the denuded alloy to air with as result a new fast oxidation. Consequently, the thermogravimetry curves showed jumps which were more or less high. In contrast the Hf–containing alloys did not encounter such oxide detachments on their surfaces. The corresponding mass gain curves were thus almost parabolic and no acceleration occurred. As revealed by the post–mortem characterization it seems that the original role of hafnium – which is ensuring the scale adherence [2, 3] – was played again by this element when it is introduced in much higher quantities than usually (here to form many carbides). The external oxide scale, which is composed of oxide of chromium and/or iron, was pegged on the alloy substrate by the HfO_2 oxides. Hafnium effectively formed such oxides, as revealed by XRD and as observed with the SEM in cross-section. In addition, when one looks at the very slow oxidation of the Hf–containing alloy, the other usual role of hafnium – which is slowing the diffusion through the scale of the species involved in the oxidation phenomenon – was also played here.

The best behavior in oxidation at 1100°C was observed with the Fh50 alloy. Additionally to the HfC carbides this alloy contained also chromium carbides. These ones acted as chromium reservoirs allowing good chromium availability in the interdendritic spaces. The chromium carbides may release chromium atoms in the interdendritic spaces which are generally considered as special diffusion paths facilitating the chromium supplying of the oxidation front. Thus the Fh50 alloy, which benefited of both HfC carbides supplying Hf, and of more chromium carbides than the Fh25 and the FH50 alloys, was particularly well helped to combat oxidation at this very high temperature of 1100°C.

5 Conclusion

Such Hf–rich iron–based alloys are potentially very interesting since, additionally to the high refractoriness of such iron–based alloys, the HfC carbides present interesting characteristics as an interdendritic repartition, a script-like shape and a good mix with the matrix. This favors good mechanical strength at high temperature. In oxidation at temperature as high as1100°C Hf also led to significant improvements of the behavior of the alloys. This was clearly demonstrated here when the slow almost parabolic mass gains obtained with the three Hf–containing alloys were compared with the ones of the Hf–free alloys containing similar chromium contents. However it is not sure that this good behavior in oxidation will remain over much longer times. Some local oxidation accelerations were effectively noticed, in the case of the FH50 alloy for example. It will be important, either to increase the volume fraction of the chromium carbides, or to increase the chromium content in the matrix. The first solution may be preferred, as demonstrated by the good performance of the Fh50 alloy and by considering the risk of precipitation of weakening sigma phase in the second case. This may be the subject of a further work.

Acknowledgments:
The authors gratefully thank Pascal Villeger who performed the XRD runs.

References:

[1] E. F. Bradley, *Superalloys: A Technical Guide*, ASM International, Metals Park **1988**.
[2] D. Young, *High Temperature Oxidation Oxidation and Corrosion of Metals*, Elsevier Corrosion Series, Amsterdam **2008**.
[3] P. Kofstad, *High Temperature Corrosion*, Elsevier Applied Science, London **1988**.
[4] M. J. Donachie, S. J. Donachie, *Superalloys: A Technical Guide* (2nd edition), ASM International, Materials Park **2002**.
[5] P. Berthod, J. Alloy Compd **2009**, *481*, 746.
[6] Y. G. Kim, J. Mater. Sci. **1978**, *13*, 759.
[7] E. Nold, G. Ondracek, *Prakt. Metallogr.* **1986**, *23,* 268.
[8] W. R. Witzke, *Metal. Trans. A* **1976**, *7A*, 443.
[9] B. L. Chen, A. Luo, K. S. Shin, D. L. Jacobson, *Refract. Metal. : State-of-the-Art, Proc. Symp. TMS Fall Meet.* **1989**, 65.
[10] A. Luo, J. J. Park, D. L. Jacobson, B. H. Tsao, M. L Ramalingam, *Scripta Metall. Mater.* **1993**, *29* , 729.
[11] A. Luo, J. J. Park, D. L. Jacobson, B. H. Tsao, M. L Ramalingam, *Mat. Sci. Eng. A-Struct.* 1994, *177*, 89.
[12] J. J. Park, D. L. Jacobson, *Tungsten Alloys, Proc. 1st Int. Conf.* **1993**, 241.
[13] J. J. Park, *Int. J. Refract. Met. H.* **1999**, *17*, 331.
[14] H. P. Gao, R. H. Zee, *J. Mater. Sci. Lett*. **2001**, *20*, 885.
[15] P. T. B. Shaffer, *Handbooks of High-Temperature materials N°1. Materials Index*, Plenum Press, New York, **1964**.
[16] P. Berthod, *Oxid. Met.* **2005**, *64*, 235.

TABLES

Table 1. Chemical compositions of the five studied alloys determined by SEM/EDS measurements (Fe: bal.; C content not assessable by EDS but assumed to be respected)

Elements / ***Alloys***	***Cr***	***C***	***Hf***
F25	26.4 ±0.3	≈ 0.25	/
Fh25	**25.8 ±0.5**	**≈ 0.25**	**4.8 ±1.8**
F50	28.4 ±1.2	≈ 0.50	/
Fh50	**25.9 ±1.1**	**≈ 0.50**	**4.0 ±0.6**
FH50	**27.5 ±0.5**	**≈ 0.50**	**5.8 ±1.2**

Table 2. Values of the classically determined Kp constant, and of the Kp and Kv constants determined using the m × dm/dt = f(m) plot

Constants	**Kp** (× 10^{-12} g^2 cm^{-4} s^{-1})	**Kv** (× 10^{-10} g cm^{-2} s^{-1})	
method	classical	m × dm/dt = f(-m)	
F25	358	/*	/*
Fh25	**8.2**	**30.4**	**147**
F50	12.4	17.5	85
Fh50	**0.4**	**2.5**	**60**
FH50	**8.1**	**25.9**	**127**

Table 3. Summary of the oxide species detected and identified in the oxide scales covering the oxidized samples

Technique / Oxidized alloy	X-ray diffraction	Energy Dispersive Spectrometry
F25	Fe_2O_3, $(\underline{Fe},Cr)_2O_3$, $FeCr_2O_3$, Cr_2O_3	Fe_2O_3, $(\underline{Fe},Cr)_2O_3$, $(\underline{Cr},Fe)_2O_3$, Cr_2O_3
Fh25	Cr_2O_3, $(\underline{Cr},Fe)_2O_3$	Cr_2O_3, $(\underline{Cr},Fe)_2O_3$, HfO_2
F50	Fe_2O_3, $(\underline{Fe},Cr)_2O_3$, $(\underline{Cr},Fe)_2O_3$, Cr_2O_3	Fe_2O_3, $(\underline{Fe},Cr)_2O_3$, $(\underline{Cr},Fe)_2O_3$, Cr_2O_3
Fh50	Cr_2O_3, $(\underline{Cr},Fe)_2O_3$, HfO_2	Cr_2O_3, $(\underline{Cr},Fe)_2O_3$, HfO_2
FH50	Fe_2O_3, $(\underline{Fe},Cr)_2O_3$, $(\underline{Cr},Fe)_2O_3$, HfO_2	$(\underline{Fe},Cr)_2O_3$, $FeCr_2O_3$, Cr_2O_3, HfO_2

FIGURES

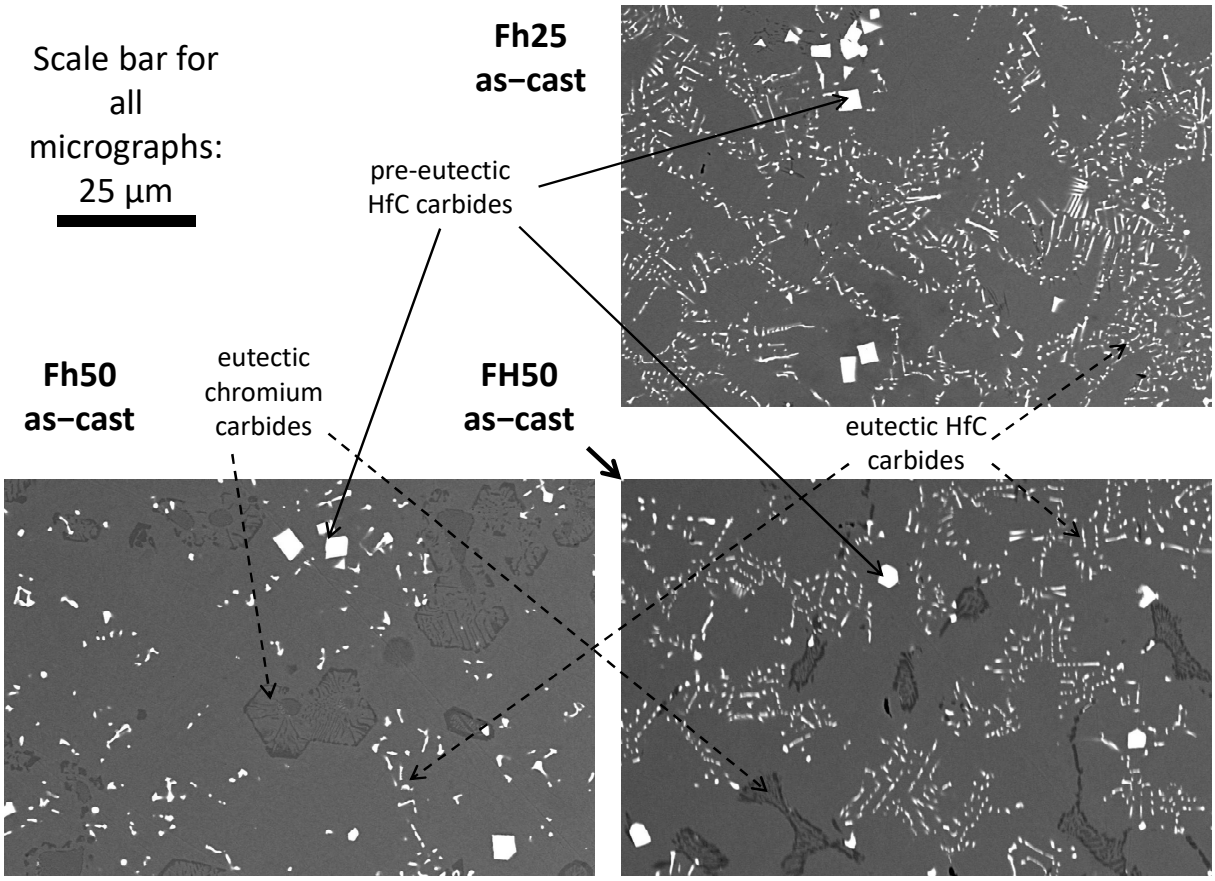

Figure 1. Microstructures of the HfC-containing alloys in the as-cast condition (SEM/BSE micrographs)

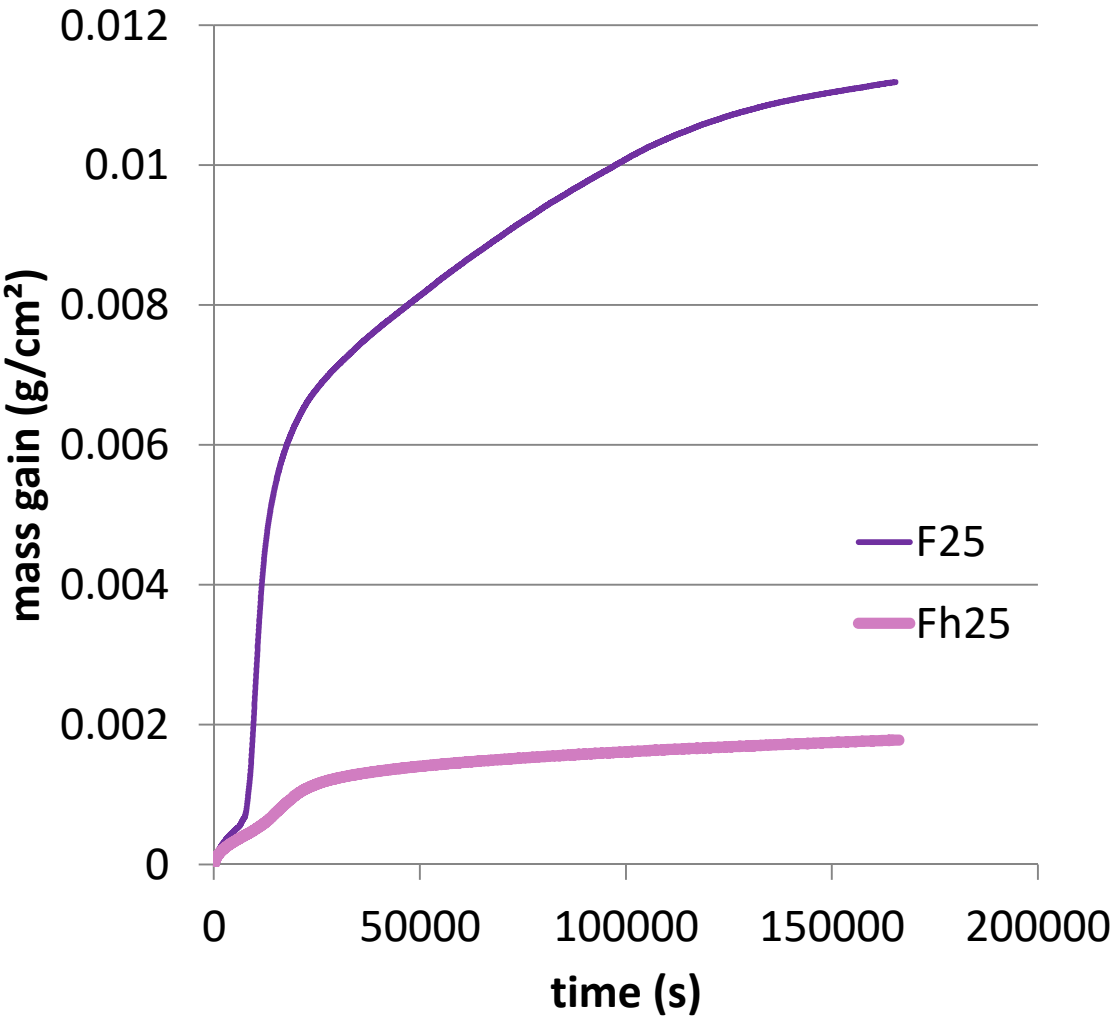

Figure 2. The mass gain curves obtained for the two 0.25 wt.%C - containing alloys (the Hf-free F25 and the Hf-containing Fh25)

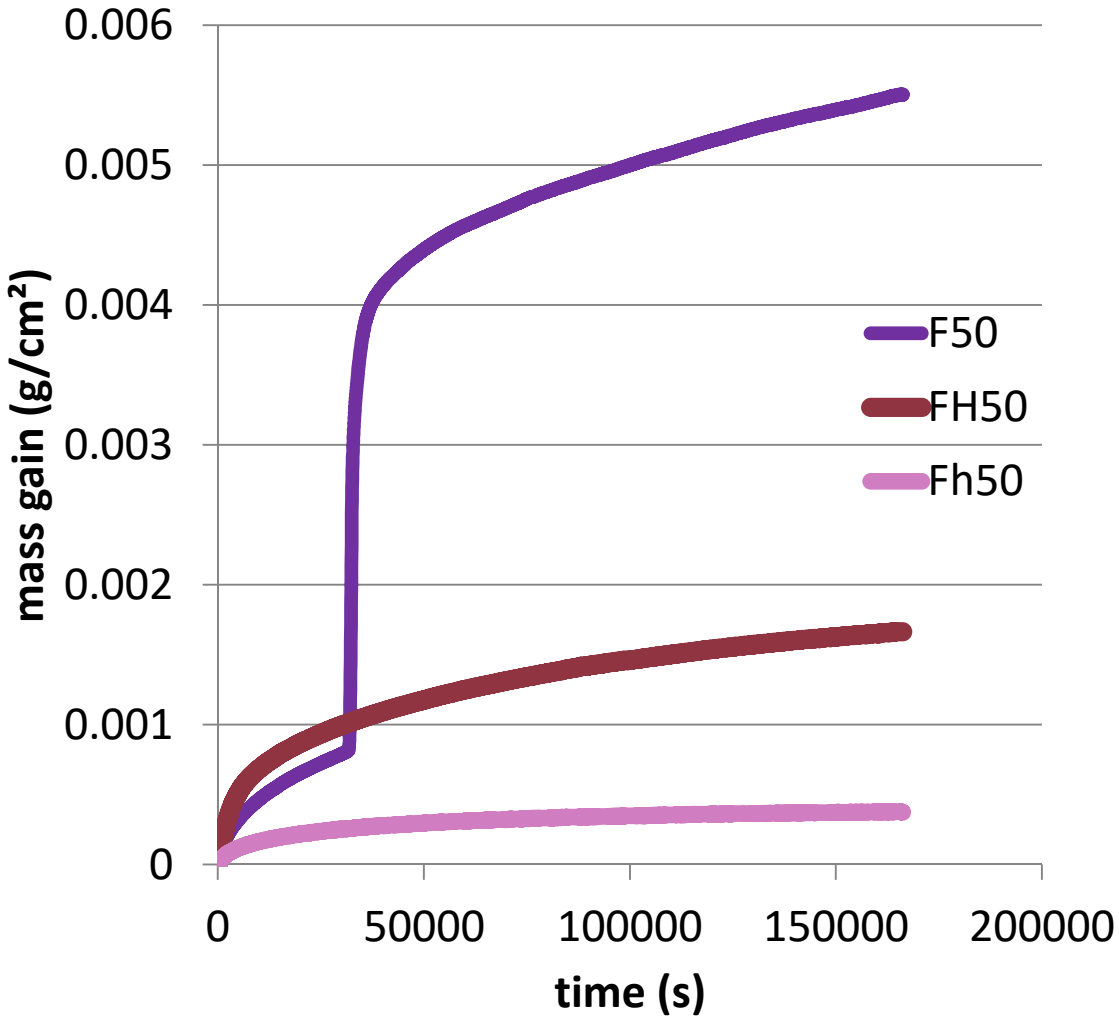

Figure 3. The mass gain curves obtained for the three 0.50 wt.%C - containing alloys (the Hf-free F50 alloy and the two Hf-containing ones: Fh50 and FH50)

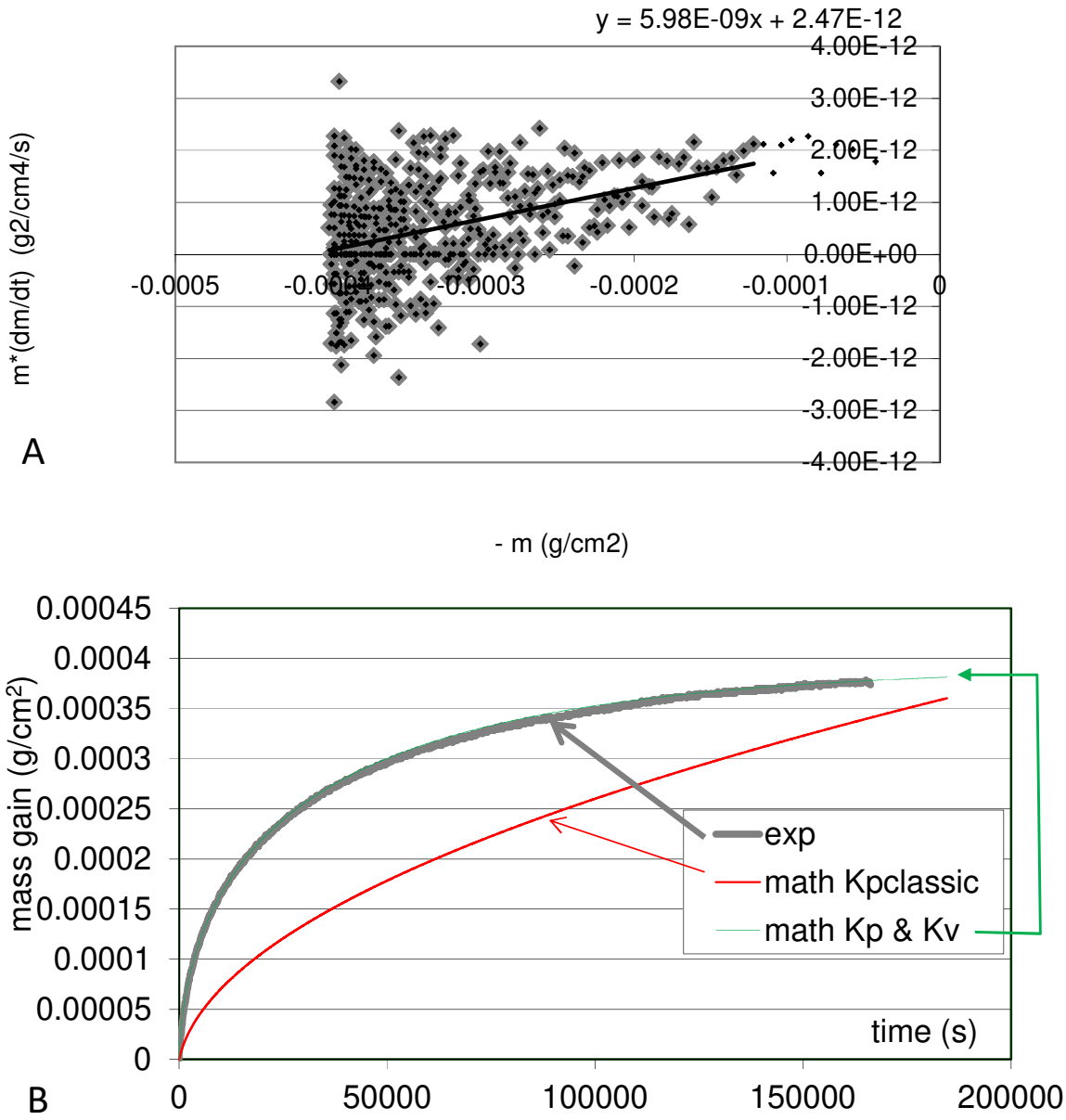

Figure 4. Example of treatment according to {m × dm/dt = Kp – Kv × m} of the mass gain files recorded by the thermo-balance during the oxidation test (here: case of the Fh50 alloy):
A: plot of the mass gain data in the {m × dm/dt = f(m)} scheme and extraction of the values of the parabolic constant Kp and of the volatilization constant Kv
B: test of the values obtained for Kp and Kv by comparing the model curve plotted with these Kp and Kv values ("math Kp & Kv") and the experimental curve ("exp"): much better fit than for a model curve plotted with the Kp value which would be found without taking into account the mass loss by chromia volatilization ("math Kpclassic")

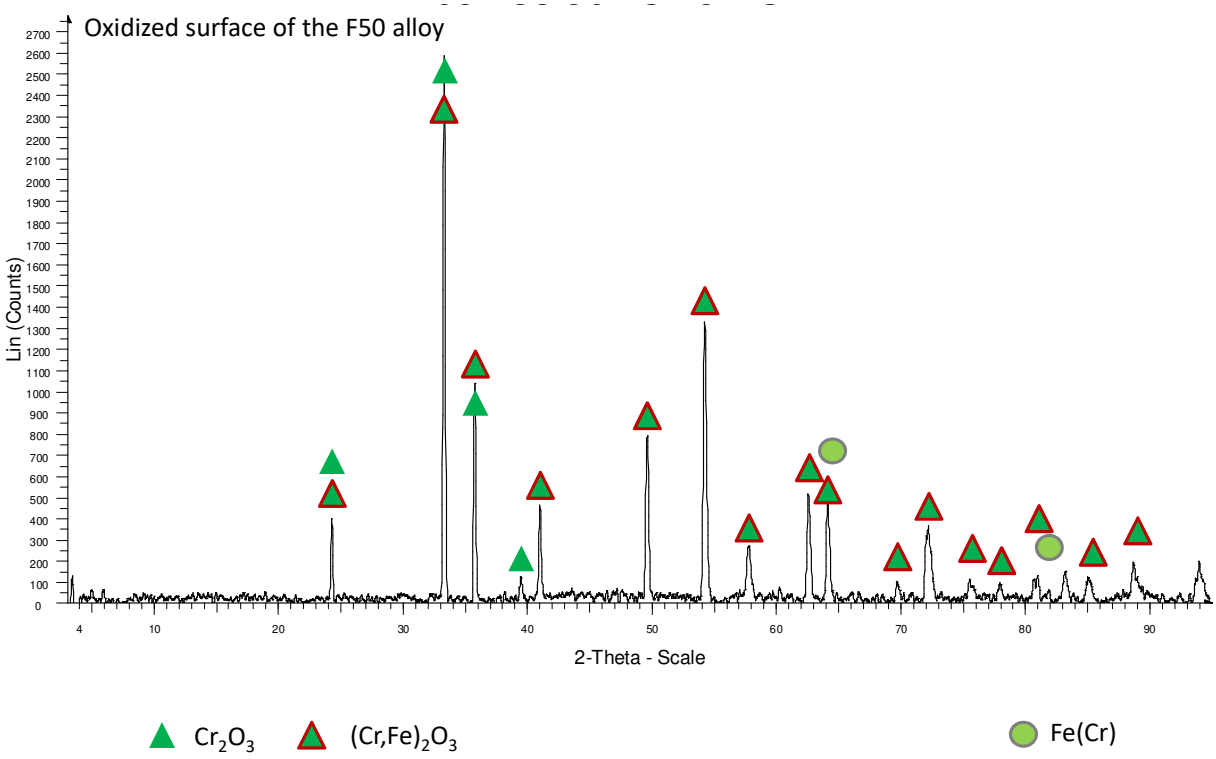

Figure 5. XRD diffractogram obtained on the oxidized surface of the F50 alloy

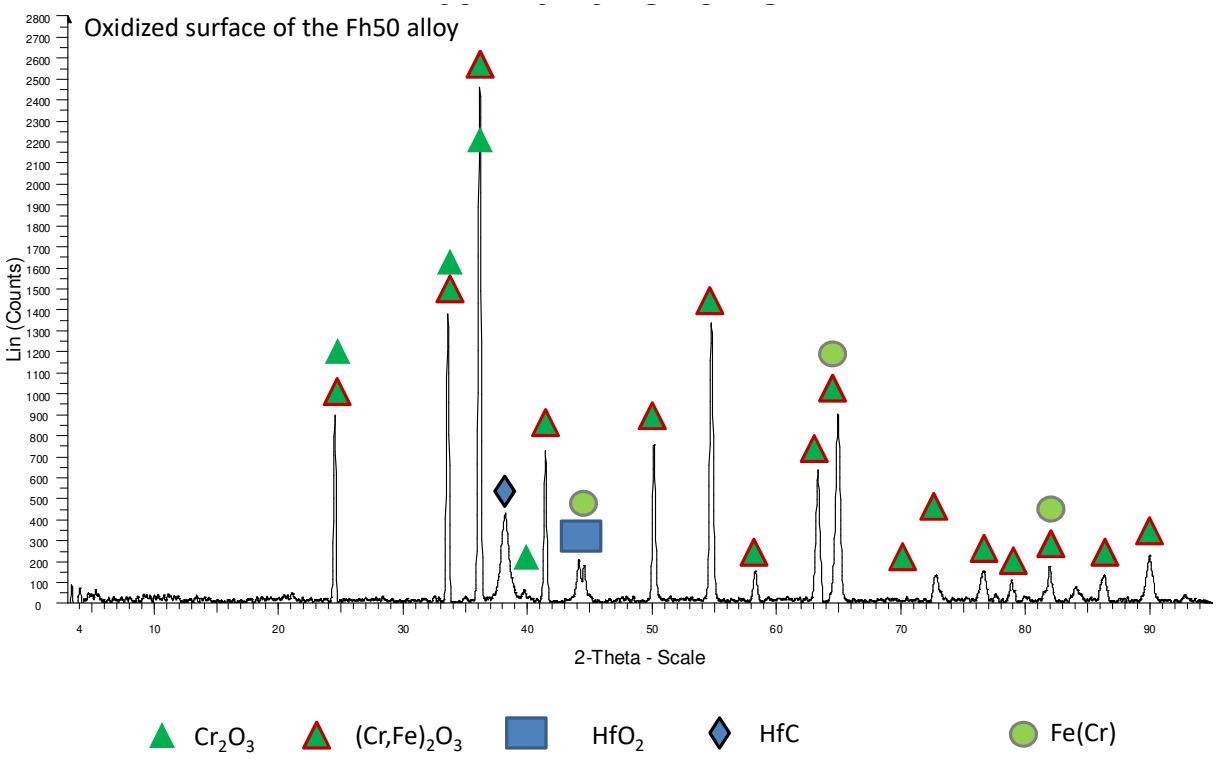

Figure 6. XRD diffractogram obtained on the oxidized surface of the Fh50 alloy

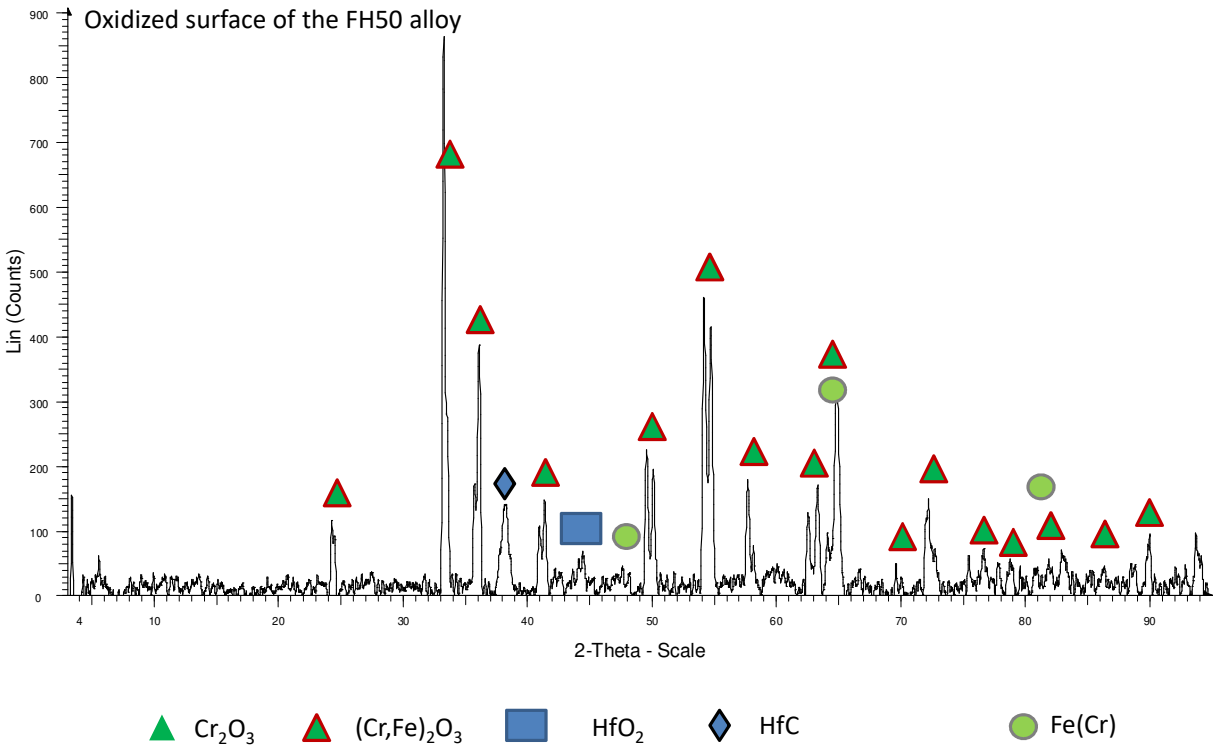

Figure 7. XRD diffractogram obtained on the oxidized surface of the FH50 alloy

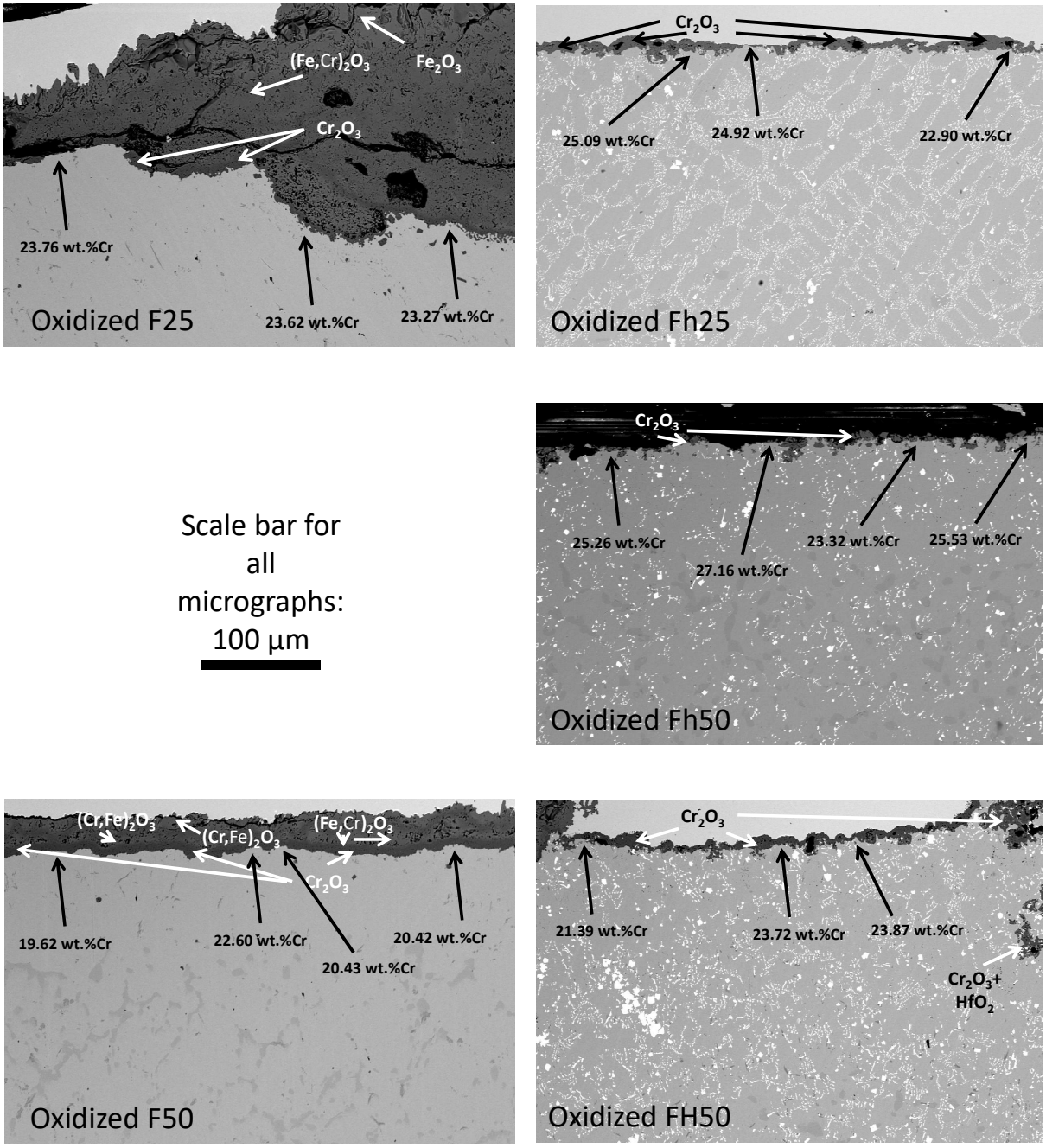

Figure 8. Surface states of the five alloys after 46 hours of oxidation in dry air at 1100°C (SEM/BSE micrographs); identified oxides (white arrows) and local chromium contents measured by EDS in alloy close to the oxidation front (black arrows)

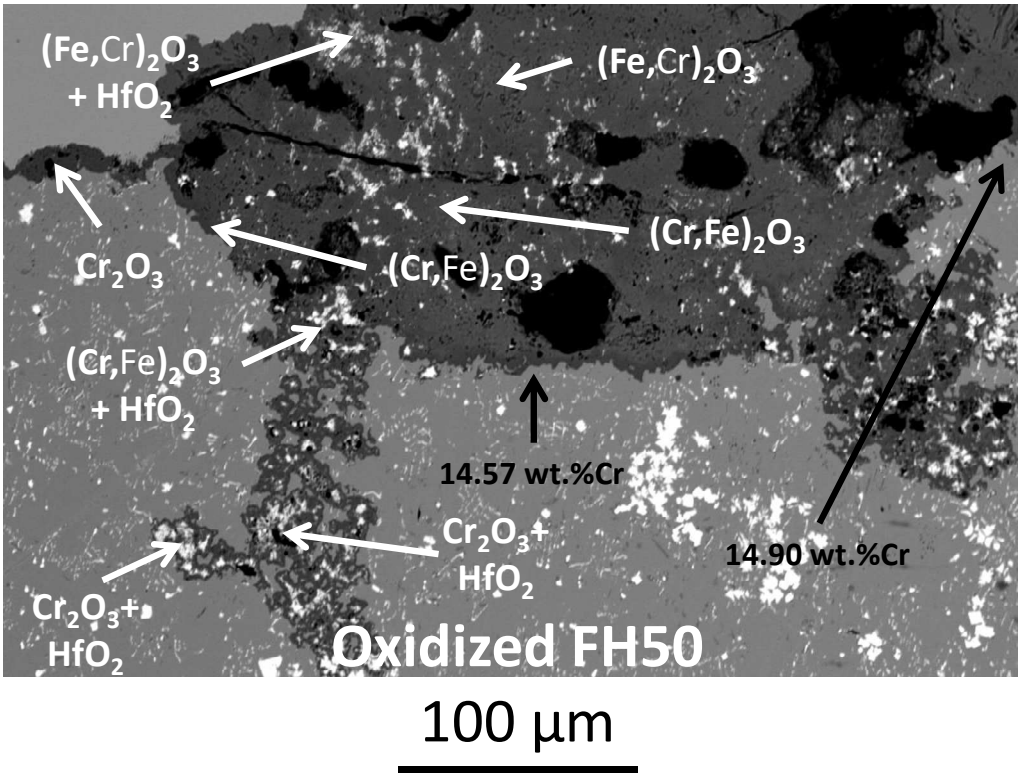

Figure 9. Analyze of a surface part of the FH50 alloy where oxidation was especially fast (SEM/EDS pinpoint analysis); identified oxides (white arrows) and local chromium contents measured by EDS in alloy close to the oxidation front (black arrows)

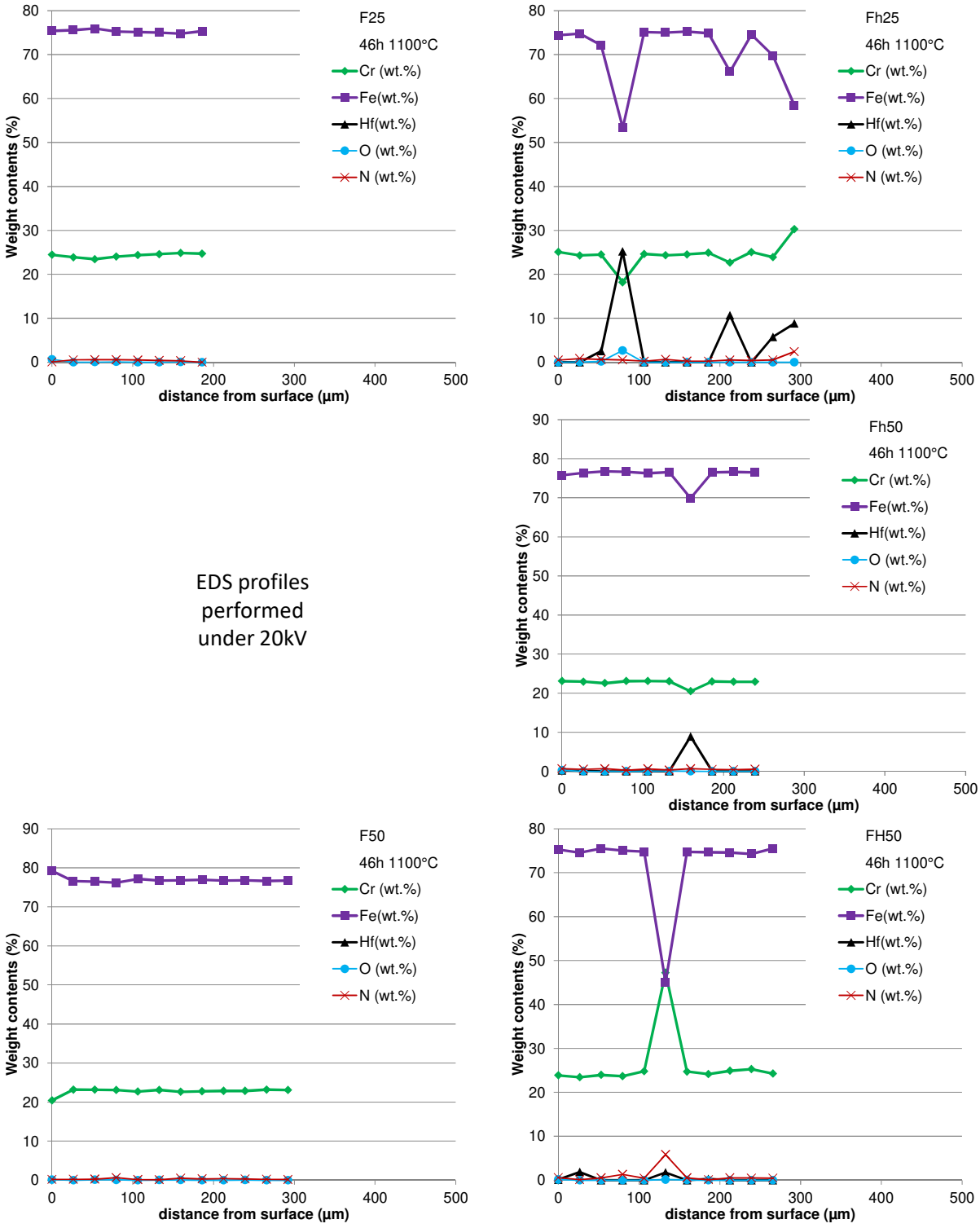

Figure 10. EDS composition profiles performed from the oxide / alloy interface (SEM/EDS pinpoint analysis)

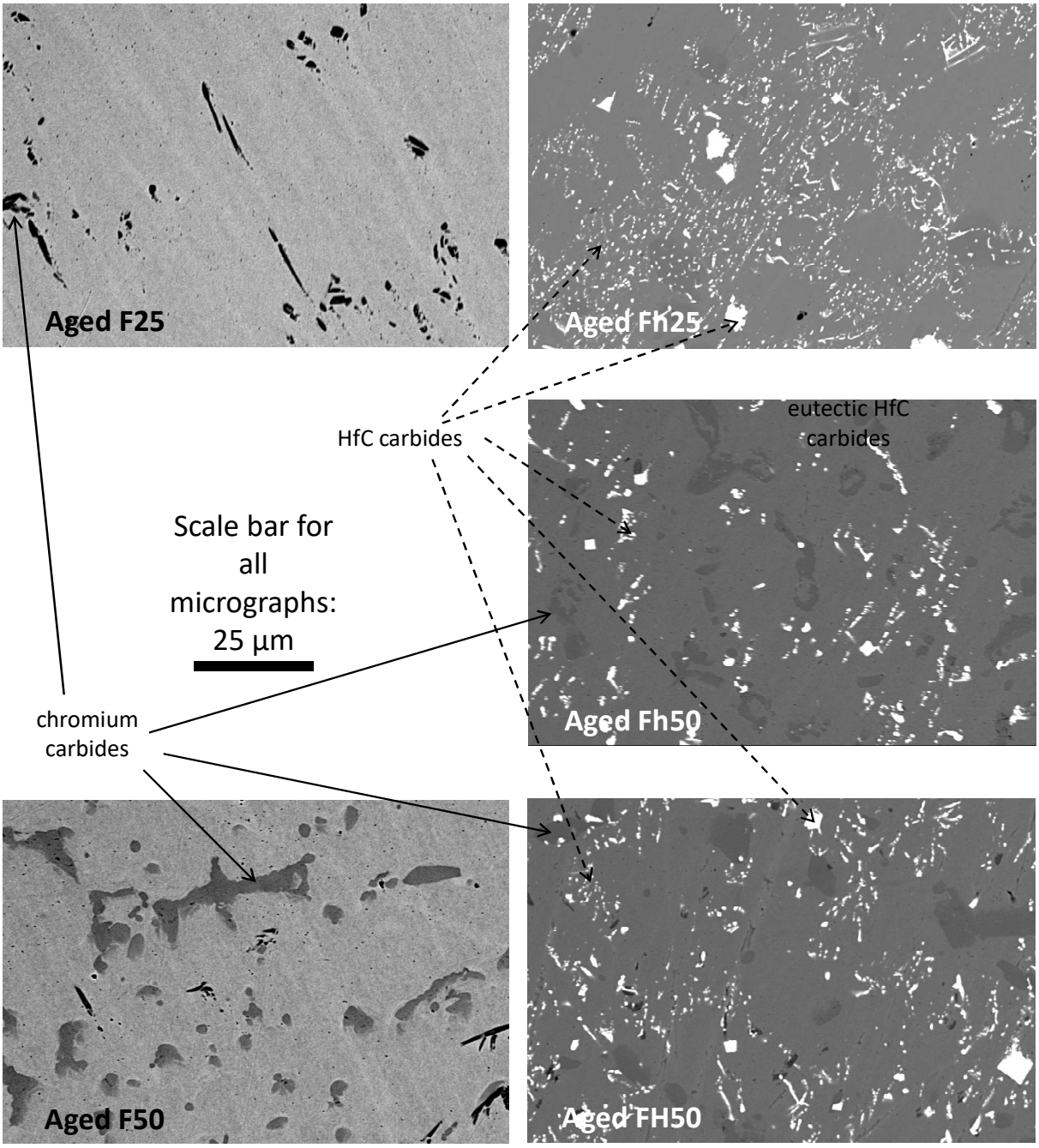

Figure 11. Microstructures of the five alloys in their bulk after 46 hours of exposure to 1100°C (SEM/BSE micrographs)